Porous Dielectric Hydrogel In MEMS Capacitive Sensors: Static And Dynamic Nonlinear Analysis

Hamzah Kadhim Hasan[1], Mina Ghanbari[2], Ghader Rezazadeh[*3,1]

[1]Mechanical Engineering Department, Urmia University, Urmia, IRAN
[2]Mech. Eng. Dept., Urmia University of Technology, Urmia, IRAN
[3]Center for Materials Technology, Skolkovo Institute of Science and Technology, Moscow, Russian Federation
Email: Inkr.hamz@atu.edu.iq
Email: m.ghanbari@uut.ac.ir, ORCID: 0000-0003-1315-9689
[*]Email: g.rezazadeh@skoltech.ru, ORCID: 0000-0001-5243-3199

Abstract

This study investigates the static and non-linear behavior of a circular microplate resting on a porous polymeric/elastomeric dielectric hydrogel foam, which fills the gap of the capacitive accelerometer sensor and is simultaneously subjected to transverse harmonic base acceleration excitation and static bias excitation. Based on the von-Karman relations and the Hamilton's principle and introducing the Airy stress function, the governing nonlinear coupled partial differential equations of the problem under fully clamped edge boundary conditions are derived and using the Galerkin's procedure are reduced to a set of nonlinear ODEs with time. Then, the validity of the formulation for analyzing the pull-in behavior of the problem achieved by comparing the obtained results with those of the literature. The static pull-in behavior of an electrostatically actuated microplate is investigated with respect to variations of the hydrogel layer parameters by solving the governed equations of multi-degree of freedom equilibrium states. In a following using the perturbation method and considering the nonlinear approximate solution of third order, the primary resonance of the problem is analyzed under the base excitation by transverse acceleration. This is done by deriving the modulation equations for the frequency response and the basic acceleration response under steady-state conditions. The existence and stability conditions of Mult-coexisting non-trivial solutions for nonlinear responses are discussed and the bifurcation points of the related characteristic curves are derived and it is shown that changes in different parameters can lead to the jump phenomenon. Performing 2-Dim and 3_Dim bifurcation diagrams and through a comprehensive analysis, the influences of the problem parameters such as bias voltage, acceleration amplitude, acceleration frequency, damping and initial volume fraction of porosity, dielectric coefficient and initial Young's modulus of the hydrogel on the nonlinear behavior of the sensor are studied and it is shown that the porosity of the hydrogel has a significant influence on the resonance amplitude.

Keywords: MEMS; Accelerometer; Nonlinear Systems, Porous Material; Frequency Response.

1. Introduction

In recent years, there have been notable advancements in the design and optimization of capacitive accelerometers. Nevertheless, there are still obstacles to overcome in addressing the nonlinear dynamics of systems that are subject to both electrostatic and mechanical forces. It is common practice to ignore the impact of porous dielectric materials and the effect of applying an AC voltage in conjunction with biasing when employing conventional methodologies. These variables give rise to intricate behavior, encompassing alterations in stiffness, resonance frequencies, and system stability. This investigation aims to address this gap in the literature by examining the collective impact of porous dielectric materials and AC voltage on the functionality and dynamic response of capacitive accelerometers.

Recently, various researchers have described the development, design, and fabrication of capacitive accelerometers utilized in different applications. Mazzei and Lellis researched to enhance the performance of monitoring systems by integrating a wireless or wired network of capacitie accelerometers [1]. The low-cost design could determine three-axis acceleration from low frequency (sun Hz) to high frequency (100 Hz) regime. Due to the importance of the accuracy, reliability, and exact sensitivity of the vibration detected by capacitive accelerometers, Chemari et al. introduced a novel modeling of a capacitive-type accelerometer based on a new formula extraction [2]. The extraction of a novel equation for selecting the damping rate under error could enhance the performance of the sensor by reducing the consumption of electrical energy and increasing the measurement accuracy by reducing the measurement error. Ghemari and Saad proposed a mathematical model for a capacitive accelerometer to improve its performance [3]. The objective of the work was to visualize the accelerometer's capacitance change concerning frequency. As the variation in capacitance affects the damping rate choice significantly, therefore a comparative study of three damping rates was performed to evaluate the sensor's performance. Simulation results could introduce the new improved- parameters capacitive sensor, a highly sensitive and reliable sensor with low measurement error and energy consumption.

MEMS (Micro-Electro-Mechanical Systems) are a combination of combine electrical and mechanical elements on a single chip. MEMS-based technology allows the production of highly compact, efficient, and often low-cost devices with various functionalities. MEMS devices can be sensors, actuators, or both, and they are used in various applications, such as medical devices, automotive systems, medical devices, aerospace, consumer electronics, and industrial equipment [4-8]. They are capable of detecting and measuring various physical phenomena such as viscosity and density of fluid [9-10], pressure [11], force and strain [12], acceleration [13], and so on. Among MEMS-based devices, capacitive MEMS accelerometers are utilized in various industrial applications due to their tiny size, high sensitivity, and low energy consumption [14-15]. Therefore, several researchers have studied the modelling, design, and performance of the micro sensors. In one of the research works, the design and analysis of a capacitive micro accelerometer were presented [16]. The presented work aimed to improve the sensor's performance by increasing its bandwidth operation. After identifying the geometric parameters of the design, a parametric analysis was performed for different acceleration values. The structural parameters were developed for an enhanced MEMS-based acceleration sensor design based on the level of their influence. Sensitivity and modal analysis were also performed to show that the operation of the developed design was better than the previous one and it was safe to operate. Thu et al. investigated the design and mathematical modelling of a single-axis MEMS accelerometer [17]. They utilized finite element analysis to achieve the mechanical stress on the silicone-sensitive element exposed to exciting acceleration in the range of 50- 300 g. It was indicated that the silicone membrane's width and length, the electrode's overlap area, and the number of comb fingers can affect the microsensor's sensitivity, significantly. In the study presented by Khouqeer et al. a MEME-based capacitive comb design with higher frequency bandwidth was introduced to record and determine the behavior of seismic waves [18]. The frequency and amplitude of vibration in the wide-band frequency structure were analyzed and compared for solid-proof mass and perforated mass. Ghanbari et al. suggested a MEMS-based capacitive acceleration sensor with a new adjustable rigidity [19]. The structure of the tuning section was made up of two fixed electrodes exposed to an adjusting voltage and two movable charge-free electrodes acting as a slider. The nonlinear rigidity in the structure is created by the generation of the electrostatic force. The stiffness tunability could enable the instrumentation to measure wide-range acceleration values. A capacitive acceleration sensor with a system with dual-spring was suggested to determine the high dynamic range acceleration [20]. The sensor which could show different sensitivities in different acceleration values could improve the dynamic sensing range by utilizing the supporting springs. The presented variable-stiffness structure could lead to the reduction of fabrication cost and increment of its reliability. Liu et al. introduced a particle swarm optimization algorithm with an orthogonal design and FEM simulation to increase the accuracy of the capacitive acceleration sensor [21]. Being time-saving and having high precision were the main advantages of the design. In another study, an accelerometer with adjustable effective rigidity generated by the electrostatic force was proposed [22]. The nonlinear dynamic behavior of the acceleration sensor was analyzed by applying the development and simulations of a theoretical model based on the pull-in dynamics. Increment of sensitivity and reduction of bias instability were the result of the sensor's experimental study.

Among several elastomer dielectric materials, polydimethylsiloxane (PDMS) has been a commonly used material in sensor technology, particularly in the fabrication of flexible and stretchable sensors due to its advantageous properties such as transparency, biocompatibility, and flexibility [23-26]. In the context of dielectric materials in sensors, PDMS can be used as an encapsulating material in capacitive sensors. In capacitive sensors, PDMS can serve as a dielectric material in the construction of the capacitive sensing element. Its flexibility allows for the fabrication of sensors that can conform to irregular surfaces or be integrated into wearable devices. PDMS-based capacitive sensors find application in various fields including biomedical sensing, environmental monitoring, and wearable technology. In capacitive sensing mechanisms, PDMS can be utilized as the dielectric layer between the movable and fixed electrodes. The accelerometer deforms in response to acceleration while maintaining electrical isolation between the electrodes due to PDMS's flexibility. Its exceptional properties make it a feasible choice for improving sensitivity, conformability, flexibility, and biocompatibility. Several types of research have been reported on applying PDMS in MEMS-based capacitive accelerometers for performance improvement. In one of the studies, a triaxial sensor for acceleration measurement has been designed and characterized for biomedical applications [27]. In the proposed symmetrical cubic design, a PDMS material placed under the mass plays the role of the spring. The structure of the sensor, its operating principle, and mathematical modelling are described in detail. For the acceleration value up to 50ms^{-2}, good linearity was obtained in the output voltage. A PDMS design modeled as a mass-spring structure with a magnetoresistive recognition method was proposed for a novel biaxial accelerometer [28]. The structure was designed for low acceleration values as motion sensing and inclination determination. No significant hysteresis was observed in the performance of the fabricated design. A wearable and flexible structure with high precision was introduced based on a multi-walled carbon nanotube [29]. The structure which was organized via vacuum filtration was applied to display the dynamic response of the beam in exposed to base-excitation. The design showed repeatability and high sensitivity in sensing human activities. A vibrotactile actuator was presented for small handheld devices based on a PDMS dielectric material [30]. In the proposed design a dielectric elastomer layer with bumps was sandwiched between layers. The generation of the electrostatic force could pull the upper layer down and cause the elastomer layer to be compressed. The vibrotactile actuator's haptic performance was analyzed by measuring the best weight ratio of the elastomer material via conducting experiments. The results indicated that a diversity of haptic sensations could be generated over the extensive frequency range.

Prior research on accelerometer sensors lacks a comprehensive analysis of multi-degree-of-freedom static pull-in behavior and nonlinear/chaotic dynamics in micro-capacitive circular plates (MCCPs) resting on a dielectric elastomeric porous hydrogel layer (PDMS foam). Specifically, the effects of combined parametric and primary forcing resonance conditions have been largely unexplored. However, studies of static pull-in and nonlinear dynamics in such acceleration sensors reveal a high sensitivity to the porous hydrogel layer's characteristics; even minor alterations in the hydrogel's porosity model can induce significant oscillations in the MCCP response. As a novel contribution, this study investigates the static pull-in instability and nonlinear/chaotic behavior of the MCCP under various resonance conditions, employing a displacement-dependent porosity and dielectric coefficient model for the hydrogel layer. Both single-mode and multi-mode analyses are used, along with a 9th-order Taylor expansion for the electrostatic and foundation forcing terms. The effects of dielectric porous elastomeric gap fillers on the nonlinear response of capacitive accelerometers are also analyzed. Through static, frequency, and base acceleration response analyses, we aim to provide valuable insights into the complex interplay between material properties, deformation, and accelerometer nonlinear behavior. This study not only contributes to the understanding of accelerometer dynamics but also offers practical implications for optimizing sensor performance in real-world applications. After deriving the governing dynamics of the problem, the present work first investigates the static pull-in behavior of a circular microplate actuated by the electrostatic force (the main part of the accelerometer sensor) resting on a porous elastomeric dielectric hydrogel concerning variations of the hydrogel media parameters. In the second stage, the non-linear transverse oscillations analysis of the microplate, which is simultaneously subjected to an electrostatic biasing voltage and a base harmonic acceleration will be performed. Then applying the third-order MSM, the influences of the different parameters, especially the porosity of the filler media on the structure's nonlinear behavior will be investigated in detail numerically. Then, under simultaneous presence of parametric and primary actuations, by preparing the frequency, voltage, acceleration and damping responses, the conditions to the existence of multi stationary solutions for the resonance amplitude and occurring dual jumping phenomena will be is analyzed. Taking into account the effects of four dominant modes and using the FFT analysis, a numerical study is also carried out to investigate the multi-periodic and chaotic behavior of the system under simultaneous primary parametric excitations, the it is showed that by increasing the excitation frequencies, the nature of the responses can change from the quasi-periodic regime to the chaotic regime and vice versa. Also, taking account the effects of four dominant modes the sensitivity of the presented capacitive accelerometer sensor with respect to the variation of the porosity volume fraction of the hydrogel layer is studied.

In this paper, we present a comprehensive static and nonlinear investigation into the effects of dielectric porous elastomeric gap fillers on the nonlinear response of the capacitive accelerometers. Through static, frequency and base acceleration response analyses, we aim to provide valuable insights into the complex interplay between material properties, deformation, and accelerometer nonlinear behavior. This study not only contributes to the understanding of accelerometer dynamics but also offers practical implications for optimizing sensor performance in real-world application. After deriving the governing dynamics of the problem, the present work first investigates the static pull-in behavior of an electrostatically actuated circular microplate (the main part of the accelerometer sensor) resting on a porous elastomeric dielectric hydrogel with respect to variations of the hydrogel media parameters. In the second stage, the non-linear transverse oscillations analysis of the microplate, which is simultaneously subjected to an electrostatic biasing voltage and a base harmonic acceleration will be performed. then applying the multiple scales method and providing the necessary bifurcation diagrams, the influences of the problem parameters, especially porosity of the filler media on the nonlinear behavior of the system will be investigated in a detail numerically.

2. Formulation of the problem

The 3-D geometric schematic of the capacitive acceleration sensor subjected to the harmonic base acceleration is depicted in Figure 1. In the proposed design with flexible clamped circular microplates (MCCP), a porous polymer layer is utilized as a dielectric material.

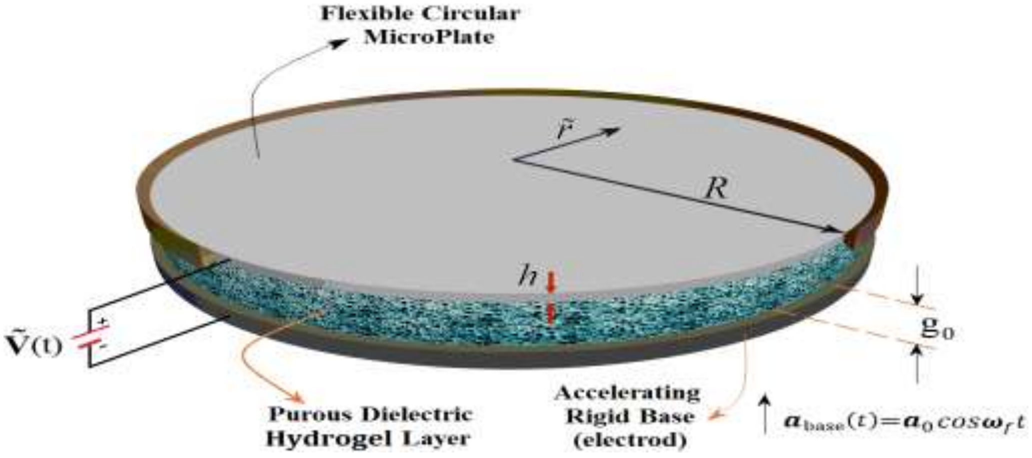

Fig.1 The 3-Dim geometric schematic of the proposed acceleration sensor with embedded porous dielectric layer exposed to biasing voltage and base acceleration.

The strain components of the microplate in radial and circumferential direction in terms of radial and transversal displacement of the plate supposing nonlinear strains in axisymmetric conditions ($\partial\tilde{\mathrm{w}}/\partial\tilde{\theta} = \partial\tilde{\mathrm{u}}/\partial\tilde{\theta} = 0$) is presented as:

$$\tilde{\varepsilon}_{rr} = \frac{\partial\tilde{u}}{\partial\tilde{r}} - z\frac{\partial^2\tilde{w}}{\partial\tilde{r}^2} + \frac{1}{2}\left(\frac{\partial\tilde{w}}{\partial\tilde{r}}\right)^2 \tag{1}$$

$$\tilde{\varepsilon}_{\theta\theta} = \frac{\tilde{u}}{\tilde{r}} - \frac{z}{\tilde{r}}\left(\frac{\partial\tilde{w}}{\partial\tilde{r}} + \frac{1}{\tilde{r}}\frac{\partial^2\tilde{w}}{\partial\tilde{r}^2}\right) \tag{2}$$

Where u and v are radial, circumferential/angular displacements and w is lateral downward deflection of the points on flexible homogeneous isotropic circular thin microplates middle surface respectively. Moreover, in the above relations, $\tilde{r}$, $\tilde{\theta}$, and $\tilde{z}$ indicate the radial, circumferential, and vertical coordinates on the microplate. Assuming that the stress-strain correlation of the microplate obeys Hook's law, one may obtain the relations between the stress and strain components as follows:

$$\tilde{\sigma}_r = \frac{E}{1-\nu^2}\left(\frac{1}{2}\left(\frac{\partial\tilde{w}}{\partial\tilde{r}}\right)^2 + \nu\frac{\tilde{u}}{\tilde{r}} - z\frac{\partial^2\tilde{w}}{\partial\tilde{r}^2} - z\frac{\nu}{\tilde{r}}\frac{\partial\tilde{w}}{\partial\tilde{r}}\right) \tag{3}$$

$$\tilde{\sigma}_\theta = \frac{E}{1-\nu^2}\left(\nu\frac{\partial\tilde{u}}{\partial\tilde{r}} + \nu\frac{1}{2}\left(\frac{\partial\tilde{w}}{\partial\tilde{r}}\right)^2 + \frac{\tilde{u}}{\tilde{r}} - \nu z\frac{\partial^2\tilde{w}}{\partial\tilde{r}^2} - \frac{z}{\tilde{r}}\frac{\partial\tilde{w}}{\partial\tilde{r}}\right) \tag{4}$$

In relations (3)-(4), E indicates Young's modulus and ν shows Poisson's ratio of the microplate. Thus, the principle of virtual displacements in polar coordinates can be represented as follows:

$$\begin{aligned}\delta W = &\int_{\tilde{t}_1}^{\tilde{t}_2}\int_{\Omega}\int_{-h/2}^{+h/2}(\tilde{\sigma}_r\delta\tilde{\varepsilon}_r + \tilde{\sigma}_\theta\delta\tilde{\varepsilon}_\theta)\,dz\tilde{r}d\tilde{r}d\tilde{\theta}d\tilde{t} \\ &- \int_{\tilde{t}_1}^{\tilde{t}_2}\int_{\Omega}\int_{-h/2}^{+h/2}\rho\left(\dot{\tilde{u}}\delta\dot{\tilde{u}} + \dot{\tilde{w}}\delta\dot{\tilde{w}} + \dot{\tilde{w}}_{base}\delta\dot{\tilde{w}}_{base}\right)dz\tilde{r}d\tilde{r}d\tilde{\theta}d\tilde{t} \\ &+ \int_{\tilde{t}_1}^{\tilde{t}_2}\int_{\Omega}\left(\tilde{P}_e(\tilde{r},\tilde{t}) - \tilde{P}_D(\tilde{r},\tilde{t})\right)\delta\tilde{w}\tilde{r}d\tilde{r}d\tilde{\theta}d\tilde{t}\end{aligned} \tag{5}$$

where W is the total work: kinetic energy, strain energy, and external work related to distributed electrostatic $\tilde{P}_e(\tilde{r},\tilde{t})$, mechanical transverse upward hydrogel pressure, $\tilde{P}_D(\tilde{r},\tilde{t})$. In (7), $\tilde{w}_{base}(t)$ is the displacement of the lower base and $\tilde{t}_1$ and $\tilde{t}_2$ are the initial and final finite times, and Ω denotes the domain of the middle plane and h represents the MCCP thickness. Knowing that the page has no motion at the beginning and end of the period $[\tilde{t}_1, \tilde{t}_2]$, using Green's theorem and some useful mathematical manipulations, the equations governing the motion of the design can be derived in an axisymmetric form as follows:

$$\frac{\partial\tilde{N}_r}{\partial\tilde{r}} + \frac{\tilde{N}_r}{\tilde{r}} - \frac{1}{\tilde{r}}\tilde{N}_\theta - I_0\ddot{\tilde{u}} = 0 \tag{6}$$

$$\begin{aligned}&\frac{1}{\tilde{r}}\frac{\partial\left(\tilde{r}\tilde{M}_r\right)}{\partial\tilde{r}} - \frac{1}{\tilde{r}}\frac{\partial\tilde{M}_\theta}{\partial\tilde{r}} + \frac{1}{\tilde{r}}\frac{\partial}{\partial\tilde{r}}\left(\tilde{r}\tilde{N}_r\frac{\partial\tilde{w}}{\partial\tilde{r}}\right) - \frac{\tilde{\tau}}{\tilde{r}}\frac{\partial}{\partial\tilde{r}}\left(\tilde{r}\frac{\partial\tilde{w}}{\partial\tilde{r}}\right) + \\ &\rho h\left(\ddot{\tilde{w}} + \ddot{\tilde{w}}_{base}\right) + 2\tilde{c}\dot{\tilde{w}} - P_e(\tilde{r},\tilde{t}) + P_D(\tilde{r},\tilde{t}) - P(\tilde{r},\tilde{t}) - \\ &I_0\ddot{\tilde{w}} + \frac{I_2}{\tilde{r}}\frac{\partial}{\partial\tilde{r}}\left(\tilde{r}\frac{\partial\ddot{\tilde{w}}}{\partial\tilde{r}}\right) = 0\end{aligned} \tag{7}$$

where c is an equivalent damping coefficient and τ is the residual stress. In the above equations, the force and moment resultants are obtained by integrating the circumferential $\tilde{\sigma}_\theta$, and radial $\tilde{\sigma}_r$, stresses over the microplate's thickness, which can be obtained as follows:

$$\tilde{N}_r = \frac{Eh}{1-\nu^2}\left(\frac{\partial \tilde{u}}{\partial \tilde{r}} + \frac{1}{2}(\frac{\partial \tilde{w}}{\partial \tilde{r}})^2 + \frac{\nu}{\tilde{r}}\tilde{u}\right) \tag{8}$$

$$\tilde{N}_\theta = \frac{Eh}{1-\nu^2}\left(\nu\frac{\partial \tilde{u}}{\partial \tilde{r}} + \frac{\nu}{2}(\frac{\partial \tilde{w}}{\partial \tilde{r}})^2 + \frac{1}{\tilde{r}}\tilde{u}\right) \tag{9}$$

$$\tilde{M}_r = -D\left(\frac{\partial^2 \tilde{w}}{\partial \tilde{r}^2} + \frac{\nu}{\tilde{r}}\frac{\partial \tilde{w}}{\partial \tilde{r}}\right) \tag{10}$$

$$\tilde{M}_\theta = -D\left(\nu\frac{\partial^2 \tilde{w}}{\partial \tilde{r}^2} + \frac{1}{\tilde{r}}\frac{\partial \tilde{w}}{\partial \tilde{r}}\right) \tag{11}$$

Where $\tilde{w}(\tilde{r},\tilde{t})$ is the lateral displacement component. E, ν, h ,and D are the elastic modulus, Poisson's ratio, thickness, and bending stiffness of the MCCP respectively. As the microplate's in-plane (radial and circumferential) stiffness is much larger than it's lateral stiffness, the in-plane vibration mode's natural frequencies will be too large compared to the natural frequencies in lateral mode. Thus, the magnitude of the in-plane displacement will be too small compared to the lateral displacement. Consequently, in low-frequency actuation regimes the effects of the inertial forces of in-plain directions can be neglected. In such a case ($\ddot{\tilde{u}} = 0$), by introducing the stress function $\tilde{\Phi}(\tilde{r},\tilde{t})$, that exactly satisfies equations (6), we can obtain the relationship between the Airy stress function and the components of the in-plane stress resultants in polar coordinates as follows:

$$\tilde{N}_r = \frac{1}{\tilde{r}}\frac{\partial \tilde{\Phi}}{\partial \tilde{r}}, \qquad \tilde{N}_\theta = \frac{\partial^2 \tilde{\Phi}}{\partial \tilde{r}^2} \tag{12}$$

Substituting Φ=Φ(r) in the (6) and (12) to (7) we get:

$$D\left(\frac{\partial^4 \tilde{w}}{\partial \tilde{r}^4} + \frac{2}{\tilde{r}}\frac{\partial^3 \tilde{w}}{\partial \tilde{r}^3} - \frac{1}{\tilde{r}^2}\frac{\partial^2 \tilde{w}}{\partial \tilde{r}^2} + \frac{1}{\tilde{r}^3}\frac{\partial \tilde{w}}{\partial \tilde{r}}\right) - \frac{1}{\tilde{r}}\frac{\partial}{\partial \tilde{r}}\left(\frac{\partial \tilde{w}}{\partial \tilde{r}}\frac{\partial \tilde{\Phi}}{\partial \tilde{r}}\right) - \frac{\tilde{\tau}}{\tilde{r}}\frac{\partial}{\partial \tilde{r}}\left(\tilde{r}\frac{\partial \tilde{w}}{\partial \tilde{r}}\right) + \rho h\left(\ddot{\tilde{w}} + \ddot{\tilde{w}}_{base}\right) + 2\tilde{c}\dot{\tilde{w}} + \tilde{P}_D(\tilde{r},\tilde{t}) - \tilde{P}_e(\tilde{r},\tilde{t}) = 0 \tag{13}$$

In addition, for the axisymmetric case, the general compatibility equation in a polar coordinate can be obtained as follows:

$$\frac{\partial^4 \tilde{\Phi}}{\partial \tilde{r}^4} + \frac{2}{\tilde{r}}\frac{\partial^3 \tilde{\Phi}}{\partial \tilde{r}^3} - \frac{1}{\tilde{r}^2}\frac{\partial^2 \tilde{\Phi}}{\partial \tilde{r}^2} + \frac{1}{\tilde{r}^3}\frac{\partial \tilde{\Phi}}{\partial \tilde{r}} = -\frac{Eh}{\tilde{r}}\frac{\partial^2 \tilde{w}}{\partial \tilde{r}^2}\frac{\partial \tilde{w}}{\partial \tilde{r}} \tag{14}$$

Equation (13) defines the pressure distribution, denoted by $\tilde{P}_D(\tilde{r},\tilde{t})$, resulting from the compression of the porous dielectric material between two electrodes. In (14), using the displacement dependent dielectric coefficient model for the hydrogel layer**,** the electrostatic pressure due to the electrical potential difference between the electrodes, $\tilde{P}_e(\tilde{r},\tilde{t})$ can be given as:

$$\tilde{P}_e = \frac{\kappa(p)\epsilon_0 \tilde{V}(\tilde{t})^2}{2(g_0 - \tilde{w}(\tilde{r},\tilde{t}))^2} \tag{15}$$

where $g_0$initial distance between electrodes is, and ϵ_0 is the vacuum electric permittivity. The applied voltage to the electrodes is indicated by $\tilde{V}(\tilde{t})$ as seen in figure 1, and $\kappa(p)$ is the hydrogel media's equivalent dielectric coefficient and is represented in terms of porosity as:

$$\kappa(p) = \kappa_p \forall_p + \kappa_s \forall_s = \kappa_p \forall_p + \kappa_s\left(1 - \forall_p\right) \tag{16}$$

The air and the dielectric material between the electrodes have dielectric constants of κ_p and κ_s in that order. The volume fraction of the porosity is denoted by $\forall_p$ and the volume fraction of the solid phase in the dielectric material is denoted by $\forall_s$.

It can be hypothesized that the deformation of hydrogel materials is caused by a reduction in porosity. That is to say, the volume of the solid portion of the dielectric material remains constant due to displacement of the microplate, and deflection occurs exclusively as a result of reduced porosity. Therefore, based on this hypothesis, the volume fraction of porosity with respect to the plate deflection, considering the radius-dependent nature of the MCCP deflection, can be defined as follows:

$$\forall_p(\widetilde{w}) = \begin{cases} \dfrac{\forall_p^{(0)} g_0 - \widetilde{w}}{g_0 - \widetilde{w}} & \forall_p^{(0)} g_0 > \widetilde{w} \\ 0 & \forall_p^{(0)} g_0 \le \widetilde{w} \end{cases} \tag{17}$$

Where $\forall_p^{(0)}$ represents the initial porosity volume fraction. Using equations (16) and (17) the electrostatic force can be rewritten as follows:

$$P_e = \left(\kappa_p\left(\forall_p^{(0)} g_0 - \widetilde{w}\right) + \kappa_s g_0\left(1 - \forall_p^{(0)}\right)\right)\frac{\varepsilon_0 \widetilde{V}^2}{2(g_0 - \widetilde{w})^3} \tag{18}$$

Since the dielectric material of hydrogel media is considered to be porous, in order to determine the compressive force exerted by the hydrogel on the microplate, therefore, using the displacement dependent porosity model one can describe the elastic modulus of the hydrogel layer in terms of porosity as follows:

$$E_D = E_D^{(0)}\left(1 - \frac{\forall_p}{\forall_p^c}\right) \tag{19}$$

where $E_D^{(0)}$ is the initial elastic modulus of the dielectric material without pores. $\forall_p^c$ is a critical porosity for which the equivalent Young's modulus is zero. Substituting (17) in (19) results in:

$$E_D(\widetilde{w}) = E_D^{(0)}\left(1 - \frac{\forall_p^{(0)} g_0 - \widetilde{w}}{\forall_p^c (g_0 - \widetilde{w})}\right) \tag{20}$$

In addition, the stress-strain relationship along the z-axis based on Hook's law can be expressed as:

$$P_D = \sigma_z = \nu_B E_D\, \epsilon_z, \qquad \epsilon_z = \widetilde{w}/g_0 \tag{21}$$

Where:

$$\nu_B = \frac{(1 - V_D)}{(1 - V_D - 2V_D^2)} \tag{22}$$

It is noted that $V_D = 0$ is corresponded to the case that the used material is a porous material. It should be noted that zeroing the Poisson ratio $V_D = 0$ or $\nu_B = 1$ corresponds to the case where the pores of the hydrogel are open. The pressure exerted by the porous hydrogel layer on the MCCP can therefore be determined using the following equation:

$$P_D = K_{ef}^{(1)}\widetilde{w} - K_{ef}^{(2)}\frac{\widetilde{w}}{(g_0 - \widetilde{w})} + K_{ef}^{(3)}\frac{(\widetilde{w})^2}{(g_0 - \widetilde{w})} \tag{23}$$

Where:

$$K_{ef}^{(1)} = \frac{E_D^{(0)} \upsilon_B}{g_0}, \quad K_{ef}^{(2)} = E_D^{(0)} \upsilon_B \frac{\forall_p^{(0)}}{\forall_p^c}, \quad K_{ef}^{(3)} = E_D^{(0)} \upsilon_B \frac{1}{\forall_p^c} \tag{24}$$

To investigate the nonlinear static and dynamic behaviors of the MCCP, specific clamped boundary conditions are defined as:

$$\widetilde{w}(R, \tilde{t}) = 0, \quad \left.\frac{\partial \widetilde{w}(\tilde{r}, \tilde{t})}{\partial \tilde{r}}\right|_{\tilde{r}=R} = 0, \quad \left.\left(\frac{\partial^2}{\partial \tilde{r}^2} - \frac{\nu}{\tilde{r}}\frac{\partial \widetilde{\Phi}(\tilde{r}, \tilde{t})}{\partial \tilde{r}}\right)\right|_{\tilde{r}=R} = 0. \tag{25}$$

Where $\widetilde{w}(0, \tilde{t})$ and $\widetilde{\Phi}(0, \tilde{t})$ are physically bounded. The above boundary conditions make the motion to be axisymmetric under an axisymmetric electro-static and mechanical forcing. It is noted that, to obtain the dimensionless form of the equations (13) and (14), Applying the following transformation:

$$r = \frac{\tilde{r}}{R}, \ w = \frac{\widetilde{w}}{g_0}, \ t = \tilde{t}\sqrt{\frac{D}{\rho h R^4}}, \ P = \frac{R^4}{g_0 D}\widetilde{P}, \ \Phi = \frac{\widetilde{\Phi}}{E h {g_0}^2}, \ w_{base} = \frac{\rho h R^4}{g_0 D}\widetilde{w}_{base}, \tag{26}$$

$$V = \sqrt{\frac{\epsilon_0 R^4}{2D {g_0}^3}}\widetilde{V}, \ \tau = \frac{hR^2}{D}\tilde{\tau}, \ c = \frac{R^2}{\sqrt{\rho h D}}\tilde{c}, \quad \beta_1 = \frac{h {g_0}^2 E}{D}, \ \beta_2 = \frac{R^4 E_D^{(0)}}{g_0 D}$$

And defining $\ddot{w}_{base} = a_{base}$ is the dimensionless acceleration of the base, the following equation in the non-dimensional form can be obtained:

$$
\begin{aligned}
&w'''' + \frac{2}{r}w''' - \frac{1}{r^2}w'' + \frac{1}{r^3}w' - \beta_1\frac{1}{r}(\Phi''w' + \Phi'w'') - \frac{\tau}{r}(w' + rw'') + \ddot{w} + 2c\dot{w} \\
&\quad + \beta_2\nu_B w - \beta_2\nu_B\frac{\forall_p^{(0)}}{\forall_p^c}\frac{w}{1-w} + \frac{\beta_2\nu_B}{\forall_p^c}\frac{w^2}{1-w} \\
&\quad - \frac{\kappa_p(\forall_p^{(0)} - w) + \kappa_s(1 - \forall_p^{(0)})}{(1-w)^3}V(t)^2 - P(r,t) + a_{base}(t) = 0
\end{aligned}
\tag{27}
$$

$$
\Phi'''' + \frac{2}{r}\Phi''' - \frac{1}{r^2}\Phi'' + \frac{1}{r^3}\Phi' = -\frac{1}{r}w''w' \tag{28}
$$

Where the prime and over dot define the derivative with respect to the r and t, respectively. Under transformation (26), the boundary conditions in non-dimensional form will be:

$$
w(1,t) = 0,\ \ w'(1,t) = 0,\ \ \Phi''(1,t) - \nu\Phi'(1,t) = 0,\ \ w(0,t) = finite,\ \ \Phi(0,t) = finite. \tag{29}
$$

Solving the coupled nonlinear equations (27) and (28) in explicit closed form while satisfying the associated boundary conditions presents significant challenges. Therefore, approximate solution methods are typically employed to address this difficulty.

$$
w(r,t) = \sum_{m=1}^{N} q_m(t)\phi_m(r) \tag{30}
$$

For this purpose, by selecting the candidate axisymmetric eigenmodes (mode shape functions) $\phi_i(r)$ corresponding to the linear $\beta_1 = \beta_2 = 0$, undamped $c = 0$, with no residual stress term $\tau = 0$ model, and setting the external electrostatic forcing $V(t)$, mechanical forcing $P(r,t)$, and base excitation $a_{base}(t)$ to zero, and considering $q_m(t) = e^{-I\omega_m t}$, by solving the following eigenvalue problem, the governing differential equation corresponding to the m'th eigenmode is achieved:

$$
\nabla^4\phi_m = \Omega_m^4\phi_m, \qquad \nabla^4 = \frac{d^4}{dr^4} + \frac{2}{r}\frac{d^3}{dr^3} - \frac{1}{r^2}\frac{d^2}{dr^2} + \frac{1}{r^3}\frac{d}{dr} \tag{31}
$$

where Ω_m refers to the m'th eigenmode nondimensional natural frequency of the free vibration. Equation (31) is known as the Bessel equation, and its solution is given by:

$$
\phi_m(r) = C_1 J_i(\Omega_m r) + C_2 Y_i(\Omega_m r) + C_3 I_i(\Omega_m r) + C_4 K_i(\Omega_m r), \quad r \le 1 \tag{32}
$$

where **J** is the first order and **Y** is the second order Bessel functions respectively. Also, **I** and **K** is the first and second order refined Bessel functions respectively. According to (31), the Bessel functions of the second type should be bounded at $r = 0$. Therefore, satisfying the accompanying boundary conditions at $r = 0$, leads the constants C_2 and C_4 be zero. By applying the clamped boundary condition associated with the edge of the MCCP and using/satisfying the orthonormality property of the shape modes as:

$$
\int_0^1 r\phi_m(r)\phi_n(r)dr = \delta_{mn} \tag{33}
$$

where δ_{mn} is the Kronecker delta function, it can be shown that the mode shapes will be as follows [31]:

$$
\phi_m(r) = \frac{J_0(\Omega_m r)}{J_0(\Omega_m)} - \frac{I_0(\Omega_m r)}{I_0(\Omega_m)} \tag{34}
$$

Substitution of the approximate solution (36) in (33) results in:

$$
\nabla^4\phi_m = -\frac{1}{r}\sum_{m=1}^{N}\sum_{n=1}^{N} q_m(t)q_n(t)\phi_m''(r)\phi_n''(r) \tag{35}
$$

In relation (35), the prime implies derivative concerning the "space variable" r. It can be shown that the simultaneous solution for Airy stress function from the equations (29) and (35) for Airy stress function, has the following form:

$$\Phi(r,t)=\sum_{m=1}^{N}\sum_{n=1}^{N}q_m(t)q_n(t)\varphi_{mn}(r) \tag{36}$$

where [31]:

$$\varphi'_{mn}(r)=\frac{1}{4r}\int_0^r \eta\phi'_m(\eta)\phi'_n(\eta)d\eta+\frac{r}{4}\int_r^r\frac{\phi'_m(\eta)\phi'_n(\eta)}{\eta}d\eta+\frac{r}{4}\frac{1+\nu}{1-\nu}\int_0^1\eta\phi'_m(\eta)\phi'_n(\eta)d\eta, \quad m,n=1,2,\ldots,N \tag{37}$$

Subsequently, substituting equations (36) and (37) into equation (27) incorporates the influence of multi-mode effects. To manage the complexity introduced by electrostatic and foundation pressure terms, a 9th-order Taylor expansion is applied. This approximation allows for a more tractable representation of these nonlinear forces. Applying it , the equations can be expressed as:

$$\begin{aligned}\sum_{m=1}^{N}(\ddot{q}_m+2c\dot{q}_m+\omega_m^2q_m)\phi_m
&=\frac{\beta_1}{r}\sum_{m=1}^{N}\sum_{n=1}^{N}\sum_{p=1}^{N}q_mq_nq_p\left(\phi''_m\varphi'_m+\phi'_m\varphi''_{np}\right)-\frac{\tau}{r}\sum_{m=1}^{N}q_m\left(\phi''_m+\frac{1}{r}\phi'_m\right)\\
&+\beta_2\nu_B\sum_{m=1}^{N}q_m\phi_m-\beta_2\nu_B\frac{\forall_p^{(0)}}{\forall_p^c}\sum_{j=0}^{9}\left(\sum_{m=1}^{N}q_m\phi_m\right)^{j+1}\\
&+\frac{\beta_2\nu_B}{\forall_p^c}\sum_{j=0}^{9}\left(\sum_{m=1}^{N}q_m\phi_m\right)^{j+2}\\
&-\left(\left(\kappa_p\forall_p^{(0)}+\kappa_s(1-\forall_p^{(0)})\right)\sum_{j=0}^{9}a_j\left(\sum_{m=1}^{N}q_m\phi_m\right)^{j}\right.\\
&\left.-\kappa_p\sum_{j=0}^{9}a_j\left(\sum_{m=1}^{N}q_m\phi_m\right)^{j+1}\right)V(t)^2-P(r,t)+a_{base}(t)=0\end{aligned} \tag{38}$$

where the over-dot implies differentiation concerning the time and a_j's are coefficients of the Taylor expansion related to the fractional expression of the electrostatic forcing term.

Since the above governing equation contains strongly coupled nonlinear terms, thus it is very difficult and sometimes impossible to find an exact analytical explicit solution for this equation. However, referring to previous investigations, it can be noted that the effect of the vibration modes of low frequencies is more important compared to high frequencies. Therefore, to investigate the structure's nonlinear behavior, the first mode of oscillations (for simplicity let $q_1(t)=q(t)$ correspond to m=1) is used in demonstrating the single-mode nonlinear dynamics of the problem. To this end, applying the Galperin's method, i.e. multiplying each term in (38) by $r\phi_1(r)$and integrating the result over $r\in[0,1]$, and using the orthonormality property of eigenmodes, the governing nonlinear partial differential equation of the motion can be transformed into a nonlinear ordinary differential equation as follows:

$$\ddot{q}+2c\dot{q}+N(q)q=L_1V(t)^2+L_2a_{base}(t) \tag{39}$$

Where nonlinear term $N(q)$ is define as:

$$\begin{aligned}N(q) = (\alpha_1 + \alpha_2 V^2) + (\alpha_3 + \alpha_4 V^2)q + (\alpha_5 + \alpha_6 V^2)q^2 + (\alpha_7 + \alpha_8 V^2)q^3 \\ + (\alpha_9 + \alpha_{10} V^2)q^4 + (\alpha_{11} + \alpha_{12} V^2)q^5 + (\alpha_{13} + \alpha_{14} V^2)q^6 \\ + (\alpha_{15} + \alpha_{16} V^2)q^7 + (\alpha_{17} + \alpha_{18} V^2)q^8 + (\alpha_{19} + \alpha_{20} V^2)q^9 \\ + (\alpha_{21} + \alpha_{22} V^2)q^{10}\end{aligned} \tag{40}$$

By expanding the function $N(q)$ of q in the form of a Taylor series around the deformed static equilibrium state of the microplate represented by q_0, one can approximate the non-linear function $N(q)$ as follows:

$$N(q) = N(q_0) + N_1(q_0)(q - q_0) + N_2(q_0)(q - q_0)^2 + N_3(q_0)(q - q_0)^3 + \cdots \tag{41}$$

Where:

$$N_0 = N(q_0), \quad N_1(q_0) = \left.\frac{\partial N}{\partial q}\right|_{q_0}, \quad N_2(q_0) = \left.\frac{1}{2}\frac{\partial^2 N}{\partial q^2}\right|_{q_0}, \quad N_3(q_0) = \left.\frac{1}{6}\frac{\partial^3 N}{\partial q^3}\right|_{q_0} \tag{42}$$

3- Primary Resonance

Now assuming $V(t) = cte$, we analyze the nonlinear response of the accelerometer, under primary base excitation of the first mode. The base acceleration $a_{base}(t)$ is assumed tobe:

$$a_{base}(t) = a_0 cos\,(\omega_f t) \tag{43}$$

where ω_f is the external base excitation frequency. Conceptionally, when the value of the base acceleration excitation frequency (ω_f) and the system's natural frequency $(\omega_1\ )$ are close to each other, very large amplitude responses may be achieved by any small changes in accelerometer parameters. To investigate the sensor's nonlinear behavior under primary resonance conditions it is essential to consider the influence of the forcing frequency detuning parameter (σ). In this case, the relation concerning the frequency can be expressed as:

$$\omega_f = \omega_1 + \sigma\epsilon^3 \tag{44}$$

Here ϵ is a small ordering parameter used to separate and distinguish the magnitude of different terms. In (44) the frequency parameter σ indicates how far is the forced excitation frequency or base acceleration frequency from the microplate's first natural frequency. Physically, the non-dimensional DC voltage $V(t) = cte < V_{pull-in}$ makes the microplate deform towards the movable base electrode. Once the deformed state of equilibrium of the microplate has been determined, the first natural frequency, which is a function of the DC voltage, is calculated.

As shown in the previous reviews, utilizing the perturbation method for the analysis nonlinear problems leads to more accurate results compared to the other methods. So, based on the multiple scale method and assuming that dimensionless base acceleration amplitude, damping parameter, and also the nonlinear terms are small compared to linear terms; by considering the impact of a small scaling parameter ϵ related to the amplitude of the transverse vibrations of the microplate, one can order these coefficients as follows:

$$c \to \epsilon^2 c, \quad a_0 \to \epsilon^3 a_0, \quad \sigma \to \epsilon^2 \sigma \tag{45}$$

With this appropriate scaling, the forcing, damping, and nonlinearities will balance each other, making the nonlinear solution asymptotic, resulting in the modulation equation will be obtained at $O(\epsilon^3)$ and we will be able to achieve a second-order nonlinear approximation for the system. Utilizing the multiple scales method and according to the given descriptions one can consider the nonlinear second-order approximate solution for the system as follows:

$$q(t,\epsilon) = q_0(T_0,T_1,T_2) + \epsilon q_1(T_0,T_1,T_2) + \epsilon^2 q_2(T_0,T_1,T_2) + \epsilon^3 q_3(T_0,T_1,T_2) \tag{46}$$

where:

$$T_n = \epsilon^n t, \;\; n = 0,1,2 \tag{47}$$

According to the chain rule, applying the first and second-order time derivative differential operators as:

$$\frac{d}{dt}=\frac{\partial}{\partial T_0}\frac{\partial T_0}{\partial t}+\frac{\partial}{\partial T_1}\frac{\partial T_1}{\partial t}+\frac{\partial}{\partial T_2}\frac{\partial T_2}{\partial t}+\cdots=D_0+\epsilon D_1+\epsilon^2 D_2+\cdots \tag{48}$$

$$\frac{d^2}{dt^2}=(D_0+\epsilon D_1+\epsilon^2 D_2+\cdots)^2=D_0^2+2\epsilon D_0 D_1+\epsilon^2(D_1^2+2\epsilon D_0 D_2)+\cdots \tag{49}$$

Where $D_n=\partial/\partial T_n,\ (n=0{,}1{,}2)$ and substituting (46) to (51) into (41) and equating the coefficients to the same power of ϵ gives:

$$O(\epsilon^0){:}\quad N_0+L_1V_{DC}^2=0 \tag{50}$$

$$O(\epsilon^1){:}\quad D_0^2q_1+N_0q_1+N_1q_0q_1=0 \tag{51}$$

$$O(\epsilon^2){:}\quad D_0^2q_2+N_0q_2+2D_0D_1q_1+N_1q_1^2+N_1q_0q_2+N_2q_0q_1^2=0 \tag{53}$$

$$\begin{aligned}O(\epsilon^3){:}\quad & D_0^2q_3+N_0q_3+2D_0D_1q_2+2D_0D_2q_1+D_1^2q_1+N_2q_1^3+N_1q_0q_2+2N_2q_0q_1q_2\\ &+N_2q_0q_1^2+2cD_0q_1+2N_1q_1q_2+N_3q_0q_1^3+N_1q_0q_3+L_2a_0cos\,(\omega_1T_0\\ &+\sigma T_2)=0\end{aligned} \tag{54}$$

These ordered equations should be solved sequentially to obtain the non-linear response of the microplate near the resonance conditions.

4- Solutions of Ordered Equations and stability analysis

Under the circumstances when V_{DC} is less than its pull-in value $V_{DC}^{Pull-in}$, this static DC voltage will make the MCCP place a secondary deformed static equilibrium state in which in this situation a microplate bends/deforms towards the lower electrode of the accelerometer. To this end, by solving the ordered equation $O(\epsilon^1)$ with respect to q_0, the static equilibrium of the microplate is determined. Afterwards using the obtained result for q_0, the solution process moves on to solve the equations $O(\epsilon^2)$ with respect to q_1. Thus, the static equilibrium of the microplate is determined by solving the ordered equation $O(\epsilon^0)$ with respect to q_0, symbolically. Afterwards, the result obtained for q_0 is then used to solve the equations $O(\epsilon^1)$ with respect to q_1. To solve the equation $O(\epsilon^1)$ for q_1, this equation can be rearranged as:

$$O(\epsilon^1){:}\quad D_0^2q_1+\omega_1^2q_1=0 \tag{54}$$

where ω_1 represents the undamped natural frequency around the deflected configuration. With the inclusion of damping, vibrational modes that are not directly or indirectly excited will eventually decay. The long-term response of $O(\epsilon^1)$ includes the effect of modes directly excited by primary/parametric forcing or indirectly excited by the occurrence of internal resonance phenomena. Assuming that no mode exhibits internal resonance with the directly excited fundamental mode (first mode), the homogeneous solution to equation (54) can be simplified to:

$$q_1(T_0,T_1,T_2)=A_1(T_1,T_2)e^{+i\omega_1T_0}+\overline{A}_1(T_1,T_2)e^{-i\omega_1T_0} \tag{55}$$

where $A_1(T_1,T_2)$ is an unknown function, which is related to the measurement of the vibration amplitude and $\overline{A}_1(T_1,T_2)$ is its complex conjugate. Since ω_1 is known, thus we need to solve the two PDE's $O(\epsilon^2)$ and $O(\epsilon^3)$ with respect to $A_1(T_1,T_2)$ to determine q_1. In the following, by substituting (57) in $O(\epsilon^2)$ and avoiding the appearance of the secular terms on the q_2, we must have:

$$D_1A_1=\frac{\partial A_1}{\partial T_1}=0\rightarrow A_1(T_1,T_2)=A_1(T_2) \tag{56}$$

This means that the function $A_1(T_1,T_2)$ should only be a function of time scale T_2. Substituting the obtained results for q_0 and q_1 in $O(\epsilon^2)$ we can find out that the general solution $O(\epsilon^2)$ for q_2 includes a homogeneous and a particular (private) part. A simple comparison of the homogeneous solutions for q_1 and q_2 shows that they have the same form. However, unlike q_1, the solution for q_2 has not only a homogeneous part but also a particular part:

$$q_2(T_0,T_2)=b_1A_1(T_2)^2e^{+2i\omega_1T_0}+b_2\overline{A}_1(T_2)^2e^{-2i\omega_1T_0}+b_3A_1(T_2)\overline{A}_1(T_2) \tag{57}$$

Where b_1, b_2 and b_3 are the constants to be known.

Now we move on to the continuation of the solution, by substituting the obtained results for q_0, q_1 and q_2 in $O(\epsilon^3)$. Since the expression $e^{+i\omega_1 T_0}$ and its conjugate in $O(\epsilon^3)$ are part of the homogeneous solutions for q_1, therefore, to avoid the appearance of the secular terms in q_3, we must set the coefficients of this term to zero, which results in a modulation equation that corresponds to the second-order nonlinear solution as:

$$\frac{\partial A_1}{\partial T_2}+I\lambda_1 A_1(T_2)^2\overline{A}_1(T_2)+I\lambda_2 A_1(T_2)+\lambda_3 a_0 e^{I\sigma T_2}=0 \tag{58}$$

Where, λ_1, λ_2 and λ_3 are the constants to be known, and as mentioned above, a_0 is the amplitude of the forcing excitation (base acceleration). After removing the secular terms from the solution for q_3, we turn our attention to finding a non-secular solution for the $O(\epsilon^3)$. It is obvious that like $O(\epsilon^2)$ the general solution of $O(\epsilon^3)$ for q_3 contains a homogeneous and a particular part. where q_2, the solution for q_3 has not only a homogeneous part but also a private solution as the following form:

$$\begin{aligned}q_3(T_0,T_2)=&\ c_1 A_1(T_2)^2 e^{+2i\omega_2 T_0}+c_2\overline{A}_1(T_2)^2 e^{-2i\omega_2 T_0}+c_3 A_1(T_2)^3 e^{+3i\omega_2 T_0}\\&+c_4\overline{A}_1(T_2)^3 e^{-3i\omega_2 T_0}\end{aligned} \tag{59}$$

Where c_1, c_2, c_3 ,and c_4 are the constants to be determined. In following, by describing $A_1(T_2)$ in the polar coordinate as $A_1(T_2)=1/2a(T_2)e^{I\theta(T_2)}$, where $a(T_2)$ and θ(T2) are real functions and separating its imaginary and real parts after substituting into (60), and letting $\gamma(T_2)=\sigma T_2-\theta(T_2)$ one can explicitly describe the non-autonomous modulation equation in a polar representation as:

$$\dot{a}=\kappa_1 a+\kappa_2 a_0 sin\gamma \tag{60}$$

$$a\dot{\gamma}=\kappa_3\sigma a+\kappa_4 a^3+\kappa_5 a_0 cos\gamma \tag{61}$$

In the above equations, the over-dot denotes the derivative with respect to the time scale T_2. Under steady-state conditions, i.e., conditions in which the amplitude and phase of the non-autonomous modulation equation remain constant with respect to time, the equilibrium values a_{ss} and γ_{ss} can be obtained by setting $\dot{a}=0$ and $\dot{\gamma}=0$ in the (62) and (63) as follows:

$$\kappa_1 a_{ss}+\kappa_2 a_0 sin\gamma=0 \tag{62}$$

$$\kappa_3\sigma a_{ss}+\kappa_4 a_{ss}^3+\kappa_5 a_0 cos\gamma=0 \tag{63}$$

By solving the above equations numerically, it is possible to obtain the frequency response, acceleration response, and damping response of the MCCP with respect to changes in the excitation, geometrical and physical characteristics of the problem.

In the following, in order to study the stability of the obtained non-stationary steady-state solutions, we consider stable non-zero solutions for the amplitude and phase of the nonlinear system, respectively. Assuming that a_{ss} and γ_{ss} represent the algebraic equations' steady state trivial/non-trivial solutions, the general solution can be expressed as the sum of the steady state and perturbed solutions for amplitude and phase as $\boldsymbol{a}(T_2)=a_{ss}+a_p(T_2)$ and $\boldsymbol{\gamma}(T_2)=\gamma_{ss}+\gamma_p(T_2)$, where $\boldsymbol{a_p}$ and γ_p indicate the perturbed solutions of the nonlinear solutions with respect to the steady-state solutions. Substituting (66) and (67) into equations (32) and (33), and then demonstrating the related Jacobian with respect to a_p and γ_p, gives:

$$J=\left.\begin{bmatrix}\frac{\partial\dot{a}}{\partial a} & \frac{\partial\dot{a}}{\partial\gamma}\\ \frac{\partial\dot{\gamma}}{\partial a} & \frac{\partial\dot{\gamma}}{\partial\gamma}\end{bmatrix}\right|_{\substack{a=a_{ss}\\ \gamma=\gamma_{ss}}} \tag{64}$$

According to the Routh-Hurwitz stability criterion, the stability of a non-trivial stationary solution is determined by the eigenvalues of the Jacobian matrix. Specifically, stability is assured if the real parts of all eigenvalues are negative.

5- Numerical analysis of the static pull-in instability

We know that determining the pull-in voltage is very important and crucial to limit the applied bias voltage to the devices and to determine their safe/stable operating range. In flexible plates, this phenomenon happens along a certain saddle node. It is therefore necessary to determine the pull-up voltage as accurately as possible in order to fully understand the system behavior, to guide and control the stable performance of the devices, and to identify and highlight their potential limitations under different operating conditions.

This section presents a numerical analysis of the accelerometer sensor's static pull-in instability. The study investigates how variations in different problem parameters affect this instability, given a fully clamped boundary condition. Since the time-dependent terms are not important for the study of the static pull-in instability, the terms such as damping and inertia terms containing the time derivatives are set to zero. Ignoring the effect of the base acceleration $a_{base}(t)$ and letting $q_m(t)$ and $V(t)$ be independent of time, and applying the Galerkin method, equation (17) simplifies to a set of coupled multivariable nonlinear algebraic equations. This reduction facilitates further analysis and potential solution finding. In the following, the resulting equations can be solved using the multivariable Newton-Raphson method, and then; by extracting bifurcation characteristic curves, the pull-in instability of the MCCP can be studied with respect to changes in various parameters. Comparing the results with those of Vogl [32] demonstrates that incorporating the effects of three shape modes in Equation (35) adequately models the static deflection of the MCCP within its stable physical range. This suggests that the chosen model effectively captures the system's behavior. Furthermore, increasing the number of shape modes leads to convergence of the solution. This indicates that the model's accuracy improves with higher-order approximations. To validate the formulation of the microplate's static pull-in behavior, the geometrical and electromechanical properties for the first case study are selected from the published work mentioned earlier. To this end, the static pull-in behavior of a circular homogeneous microplate (without Porous Polymeric Dielectric hydrogel layer) is presented in Fig. (2) and comprehensively and rigorously validated by comparing the numerical results with those of Vogl [32]. This shows the maximum static deflection $w_{max} = w(r)|_{r=0}$ of MCCP versus the electrical forcing parameter V^2 for $\nu = 0.3$, $\tau = 0$, $\beta = 1$,and two specific values $N = 1$ and $N = 3$. As its seen in Figure (2), the characteristic curves include the lower and upper branches of static solutions for the maximum deflection of the microplate versus the variation of V^2, where the lower and upper branches correspond to stable and unstable solutions, respectively. The results presented in the figure demonstrate a strong agreement between the referenced results and those obtained using the current model.

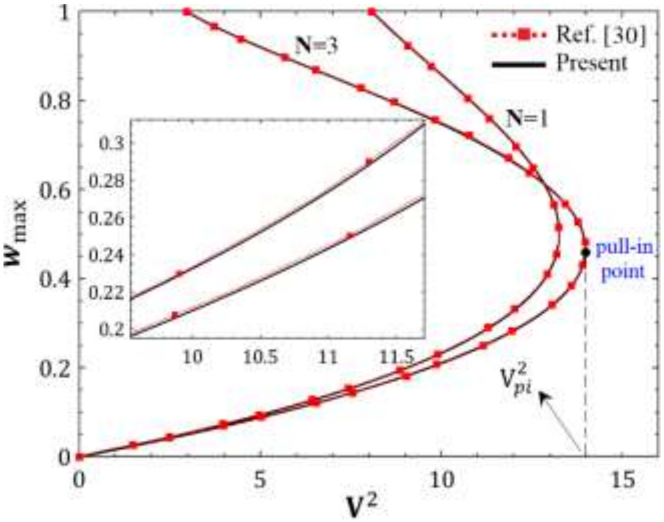

Fig 2. The maximum deflection of the microplate the variation of V^2
comparison between the present work and Ref. [32].

In the present investigation, our aim is to analyze the effects of changes in the parameters of a porous polymeric hydrogel layer on the static pull-in characteristics (in-stability) of the microplate. For this purpose, unless otherwise stated, the material properties of the microplate and the polymeric porous hydrogel are assumed to be those given in Table 1.

Table 1. Geometrical and physical properties of the problem.

Parameter	Symbol	Value
The radius of MCCP	R	$500\ \mu m$
Porous dielectric hydrogel Thickness	g_0	$4\ \mu m$
MCCP thickness	h	$5\ \mu m$
MCCP Young's Modulus	E	$169\ GPa$
Poison's ratio	ν	0.25
MCCP density	ρ	
Porous Polymer material Young's Modulus	E	
residual stress	τ	1
Initial Young's modulus of the dielectric material	$E_D^{(0)}$	$300\ KPa$
The initial volume fraction of polymer porosity	$V_P^{(0)}$	0.05
dielectric coefficients of air	k_p	1.0006
dielectric coefficients of hydrogel layer	k_s	30
Critical Porosity of polymeric hydrogel layer	$V_P^{(c)}$	0.05

From Figure 3, it can understand that an increase in the initial porosity volume fraction of the hydrogel, $\forall_p^{(0)}$, has a softening effect and reduces the stiffness of the MCCP, which in turn reduces the static pull-in of the MCCP. It means that the MCCP deflects more as $\forall_p^{(0)}$ increases. In addition, this figure illustrates that the variation of pull-in voltage with initial porosity volume fraction, $\forall_p^{(0)}$, is very much, while maximum deflection at the pull-in point has a small variation with $\forall_p^{(0)}$.

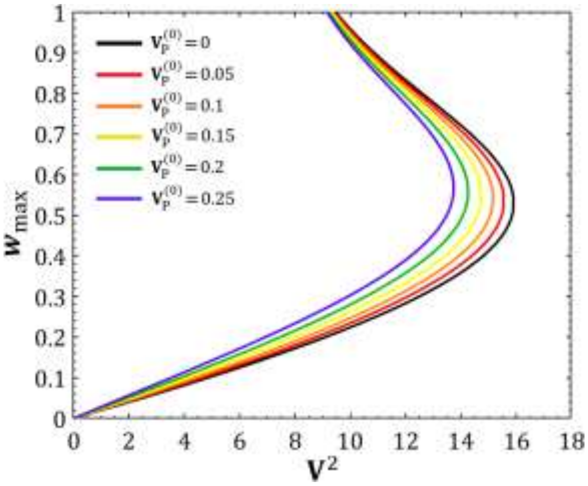

Fig 3. The maximum deflection of the clamped edge MCCP versus the V^2 for various initial porosity volume fraction.

In Figure (**4-a**) the influence of changing the initial Young's modulus of the dielectric hydrogel foam $E_D^{(0)}$, on the pull-in voltage is illustrated. Variations in the center deflection of the MCCP versus changes in V^2 for six values of the initial elastic modulus of the hydrogel foam shows that an increase in $E_D^{(0)}$, has a hardening influence on the system. This variation not only causes the stiffness of the microplate to increase but also makes the static pull-in voltage of the microplate increase. The equilibrium curves, in which the variations of the microplate center static deflection versus the square of the electrostatic voltage are indicated in Figure (**4-b**) considering different values of the hydrogel layer dielectric coefficient dielectric coefficient, k_s, of the hydrogel layer, show that an increase in k_s has a softening influence on the microplate. This implies that an increase in k_s leads to a dual effect: a reduction in the microplate's stiffness and a decrease in its static pull-in voltage.

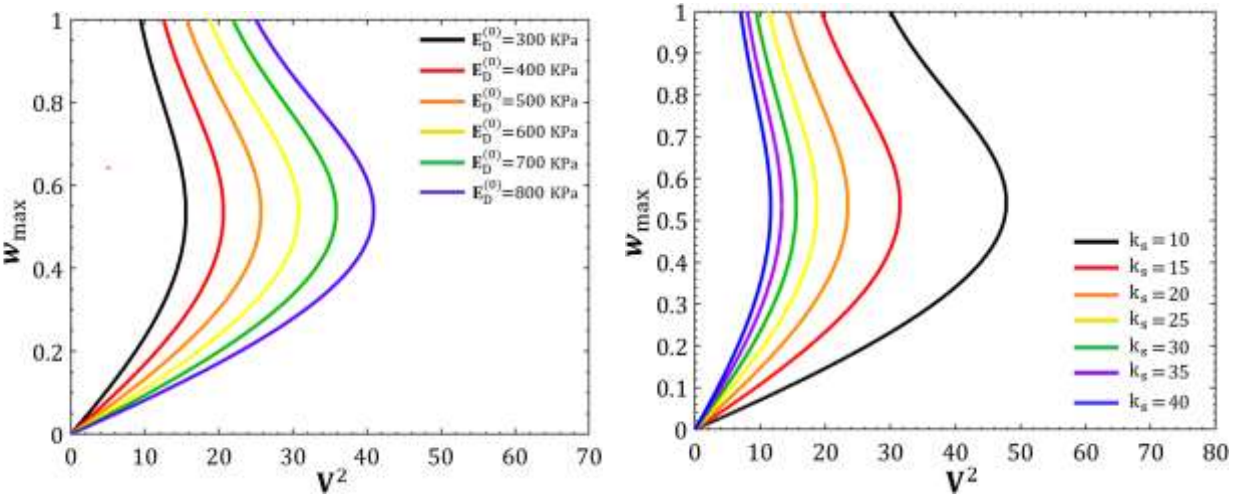

(a) **(b)**

Fig 4. Variations of the maximum static defection versus the V^2 for six values of:
(a), initial Young's modulus $\boldsymbol{E}_D^{(0)}$, **(b)** dielectric coefficient k_s of the hydrogel layer.

6- Parametric study on a designed capacitive accelerometer sensor

In the following, to study the sensitivity of the designed capacitive accelerometer sensor under the actuation of the base by the constant acceleration a_0, neglecting the time dependent terms, a numerical study is performed using the effects of four dominant modes to approximate the transverse displacements of the MCCP deflection as:

$$w(r) = \sum_{m=1}^{4} q_m \big(J_0(\Omega_m r)/J_0(\Omega_m) - I_0(\Omega_m r)/I_0(\Omega_m)\big) \tag{65}$$

Where $\Omega_1 = 3.1962206$, $\Omega_2 = 6.306437$, $\Omega_3 = 9.439499$ and $\Omega_4 = 12.577130$ and q_m is static amplitude of the m'th mode. Considering effects of abovementioned modes and by substituting (65) into (36) and (38) and utilizing the Galerkin's method, the governing nonlinear equations of MCCP static deflection are derived and, using the multi variable newton Raphson method, the obtained nonlinear algebraic equations were solved numerically. In the following, using the above approximated solution for plate static deformation, $w(r)$, one can obtain the capacitance of the accelerometer sensor as a bellows:

$$C = 2\pi \int_0^R \left[\frac{\kappa_p(\forall_p^{(0)} g_0 - w) + \kappa_s g_0 (1 - \forall_p^{(0)})}{g_0 - w}\right] \frac{1}{g_0 - w(r)} r\, dr \tag{66}$$

Figure 5 demonstrates the variation of the dimensionless capacitive sensitivity versus the dimensionless base acceleration a_0 for six values of the initial porosity volume fraction, $\forall_p^{(0)}$, of the hydrogel layer. It is evident from the figure that the capacitive sensitivity curves undergo a concurrent shift upwards and to the left as $\forall_p^{(0)}$ increases. This indicates a heightened responsiveness of the capacitive sensitivity to changes in porosity, and a lower collapse critical a_0 results in a higher $\forall_p^{(0)}$. Consequently, an increase in the $\forall_p^{(0)}$ exerts a dual effect on the capacitive sensitivity, leading to an increasing in sensitivity as well as an degradation in the a_0 sensing range, defined as the measurable base acceleration range.

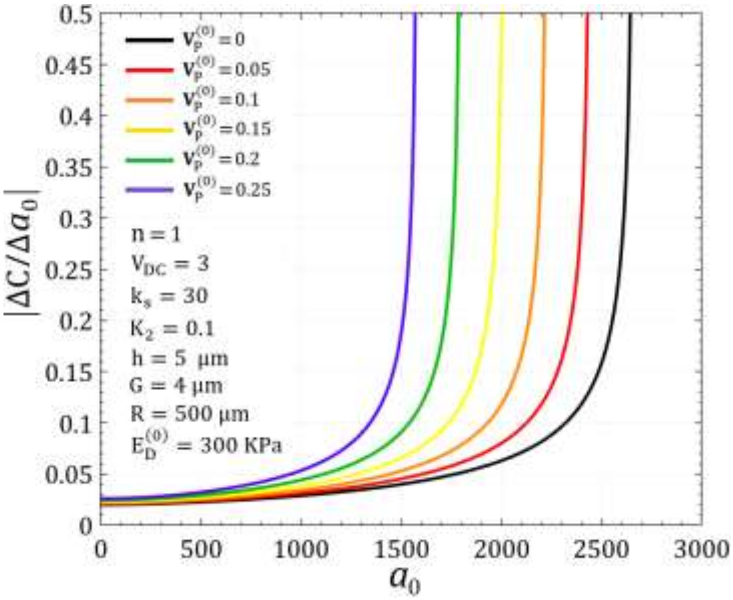

Fig 5. Variations of the dimensionless $|\Delta C/\Delta a_0|$ versus the dimensionless base acceleration a_0 for six values $\forall_p^{(0)}$.

7- Numerical results for Nonlinear behavior

The variation of the resonance amplitude of the micro capacitive circular microplate (MCCP) versus the excitation frequency, including the damping effect, is shown in Figure (**6-a**). In this figure, the characteristic curves of the frequency response have been drawn, showing the hysteretic hardening type behavior, where the continuous curves represent non-trivial stable solutions and the dashed curves represent unstable non-trivial solutions. In region I, When the excitation frequency of the base acceleration, $\boldsymbol{\omega_f}$, exceeds the structure's natural frequency $\omega_1 = 50.857$ (point **A**), only a non-trivial stable solution for the resonance amplitude exists. This results in the microplate oscillating with a small amplitude. As the excitation frequency gradually increases from point A towards the left, the amplitude of this stable non-stationary solution also increases continuously and gradually. In the following, approaching the excitation frequency to the first natural frequency (corresponding to $\sigma\epsilon^3 = 0$), leads to the increment of the stable non-stationary solution's amplitude until it reaches point C with a relatively steep high slope. After passing through the saddle-like bifurcation point, the branch representing the unstable non-zero solution bifurcates backward. Essentially, this type of bifurcation causes a jump phenomenon where the structure's non-linear response amplitude drops (decreases) sharply from point C to a stable non-zero solution at point C'.

According to Figure (**6-a**), in Region **III**, as the excitation frequency continues to decrease, the resonance amplitude or the amplitude of the non-linear response of the micro-plate, gradually and continuously decreases with a gentle slope (from point C' to point D). Conversely, as the value of actuating frequency increases gradually from point D along the DC'B' path, the resonance amplitude increases continuously until it reaches the second saddle-shaped forked point, i.e., point B'. At this point, the resonance amplitude suddenly increases to the value corresponding to the stable non-stationary solution, i.e., point B. As the process of decreasing the excitation frequency from point B to point A continues, the resonance amplitude of the system also decreases continuously. As a result, Figure (**6-a**) shows that the behavior of the accelerometer studied around its fundamental frequency will have two bifurcation points of a destructive nature at points C and B'. The accelerometer will therefore react differently at the excitation frequencies corresponding to these points, so that near point C, a small decrease in the excitation frequency will also cause the resonance amplitude of the system to decrease suddenly. Also, at point B', a slight/small decrease in the base excitation frequency will cause a sudden increase or jump in the amplitude of the non-linear response. The simultaneous existence of dual non-stationary stable solutions for the nonlinear response near the fundamental frequency causes hysteretic type characteristics to appear during the $\mathrm{ABCC'D}$ and $\mathrm{DC'B'BA}$ paths. This figure indicates that in the approximate frequency range of $31 \leq \omega_1 \leq 42$, for the resonance amplitude ,there will appear two stable and one unstable non-stationary solution (region **II**). Therefore, in this bi-stable frequency range, the non-linear response of the accelerometer will depend on the initial conditions such that the resonance amplitude can attract one of the non-linear responses.

Corresponding to the dimensionless values $a_0\epsilon^3 = 42,\ c\epsilon^2 = 9$ and $\omega = 45$, the phase trajectories of the problem (i.e., the solution curves) are plotted in the (**γ-a**) plane, known as the phase plane (Figure **6-b**). The trajectories of the problem in such a phase portrait are marked with arrows to indicate the direction of the increase in time. According to this figure, two stable spiral points P_1 and P_3 correspond to the lower and upper branches of the frequency response curves (lower and upper stable solutions in Figure **6-a** and **6-b**. In addition, the un-stable saddle point P_2 is related to the unstable resonance amplitude solution on the middle branch of the frequency response curves. It can be seen that the domain of attraction of the stationary stable responses P_1 and P_3 are separated by separator (separating boundaries) at the unstable saddle-like point P_2. So, according to the associated initial conditions, the time responses will follow the trajectories until placed in the corresponding stable situations.

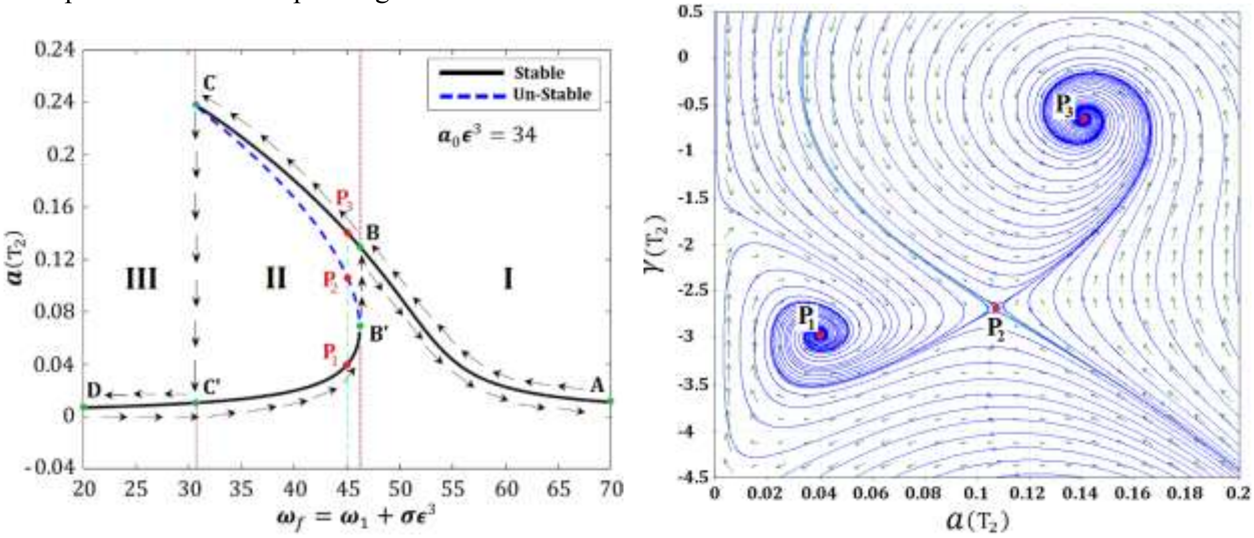

(**a**) (**b**)

Fig. **6**: (**a**), Frequency response for a given perturbed acceleration $a_0\epsilon^3 = 34$,
(**b**) Phase Plane trajectories of the problem for $a_0\epsilon^3 = 34$.

Figure 7(a) illustrates the relationship between resonance amplitude and the base actuating frequency for five distinct values of the dimensionless perturbed acceleration amplitudes. From this figure it can be found that for $a_0\epsilon^3 = 2$ and $a_0\epsilon^3 = 10$, only one stable non-zero solution will appear for the nonlinear amplitude. This figure also shows that when the applied base actuating acceleration is small, the microplate will resonate with a small amplitude, as expected.

Two saddle node bifurcation points emerge, delineating a bi-stable region when the base acceleration is sufficiently large. An increase in the actuating acceleration amplitude leads to a general rise in the structure's resonance amplitude. This means the system responds more intensely as the driving force becomes stronger. Consequently, as the excitation amplitude increases, the magnitude of the jump up or jump down phenomenon is significantly amplified. It can be observed that by increasing the vibration amplitude of the design, the width of the triple response region (resonance region) and the resonance amplitude increase. Examination of Figure (**7-b**), where the resonance amplitude $\boldsymbol{a}(T_2)$ is plotted against the excitation frequency considering different values of the initial porosity volume fraction, $\forall_p^{(0)}$, of the dielectric layer and certain value of dimensionless electrostatic DC voltage $\boldsymbol{V} = 3.5$ (below the associated pull-in voltage), shows that increasing of $\forall_p^{(0)}$ increases the resonance amplitude. Because with the increase of $\forall_p^{(0)}$, the characteristic curves of the frequency response bend towards the upright position, consequently, the instability region's width corresponding to the existence of two non-zero dual stationary solutions for $\boldsymbol{a}(T_2)$ is reduced.

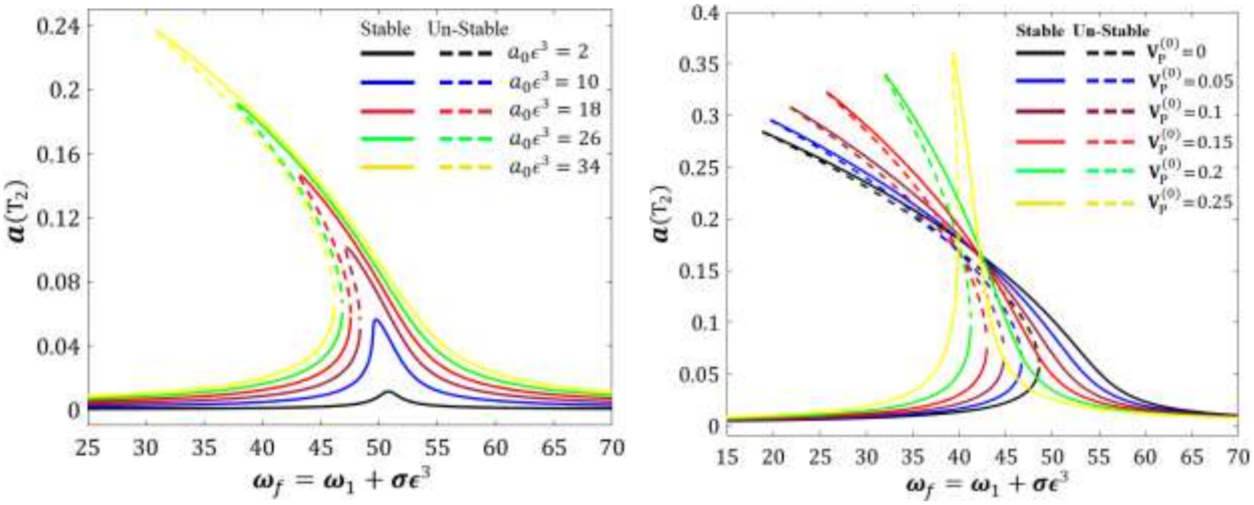

(**a**) (**b**)

Fig. **7**: Frequency response for: (**a**), five six values for the perturbed amplitude of base acceleration, (**b**) values of the initial porosity volume fraction $\forall_p^{(0)}$.

Figure (**8-a**) shows the frequency response for five values of $E_p^{(0)}$ of the hydrogel layer. As mentioned before $E_p^{(0)}$is the elastic modulus of the dielectric hydrogel when there is no porosity. It is clear from this figure that increasing of $E_p^{(0)}$ increases the sensor's non-linear softening behavior. It means that as $E_p^{(0)}$ increases, the characteristic curves become more curved to the left and the distance between the bifurcation points of these curves becomes greater. This results in an expansion of the region's width, which corresponds to the presence of multiple non-trivial stationary solutions for the resonance amplitude. This indicates that a broader range of conditions now supports diverse and stable states within the system. The design's response in the frequency domain for five values of the dielectric coefficient k_s, of the hydrogel layer is shown in Figure (**8-b**). An increase in the dielectric coefficient of the hydrogel layer results in a shift of the bifurcation points to the right. As a consequence, the bi-stable resonance region, which is associated with catastrophic hysteretic behavior, tends to diminish.

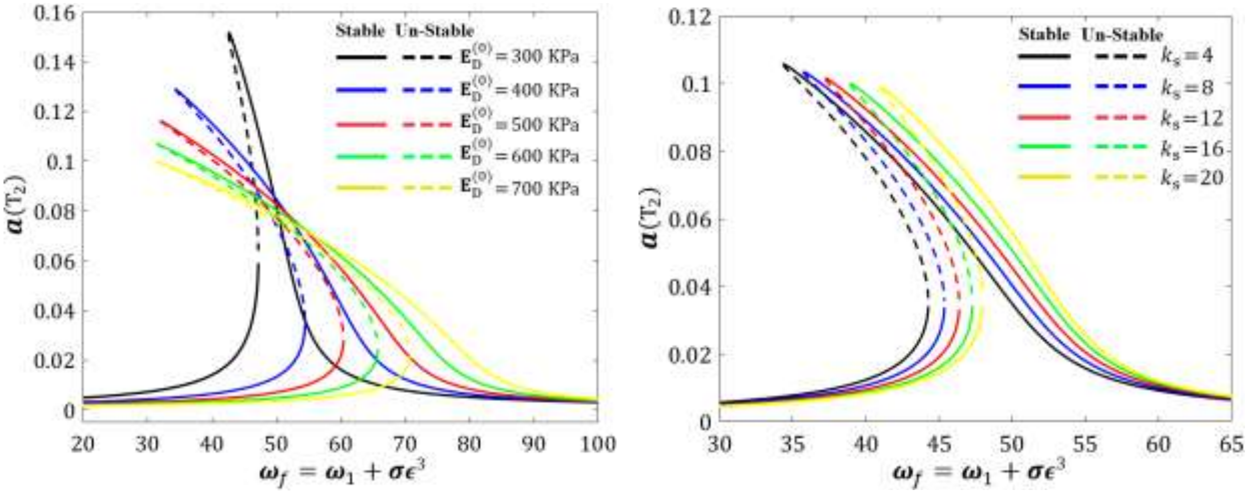

(**a**) (**b**)

Fig. **8**: Frequency response for: (**a**) five values of the initial modulus $E_p^{(0)}$,
(**b**) five values of the dielectric coefficient of the hydrogel layer, k_s.

The resonance amplitude versus the perturbed base acceleration $a_0\epsilon^2$ which is known as acceleration-response characteristic curves is depicted in figure (**9-a**) for a six value of dimensionless perturbed damping parameter$c\epsilon^2$. According to this figure, it can be seen that the resonance of the MCCP is always excited, whether damping exists or not, and an increase in $a_0\epsilon^2$ results in an overall increase in the resonance amplitude. As shown in the figure, an increase in the damping parameter $c\epsilon^2$ causes a reduction in the resonance amplitude. This increase also shifts the saddle-like bifurcation points to the right, bringing them closer together. Consequently, the bi-stable region, characterized by triple solutions for the resonance amplitude and indicative of hysteretic behavior, tends to decrease. Figure (**9-b**) shows the variations of the $\boldsymbol{a}(T_2)$ versus the variations of the perturbed base acceleration $a_0\epsilon^2$ considering different values of the initial porosity volume fraction, $\forall_p^{(0)}$, of the hydrogel and dimensionless biasing DC voltage $V = 3.5$. According to this figure, increasing the $\forall_p^{(0)}$ not only increases the resonance amplitude but also causes the shift of the bifurcation points to the right, so that the bi-stable region tends to increase.

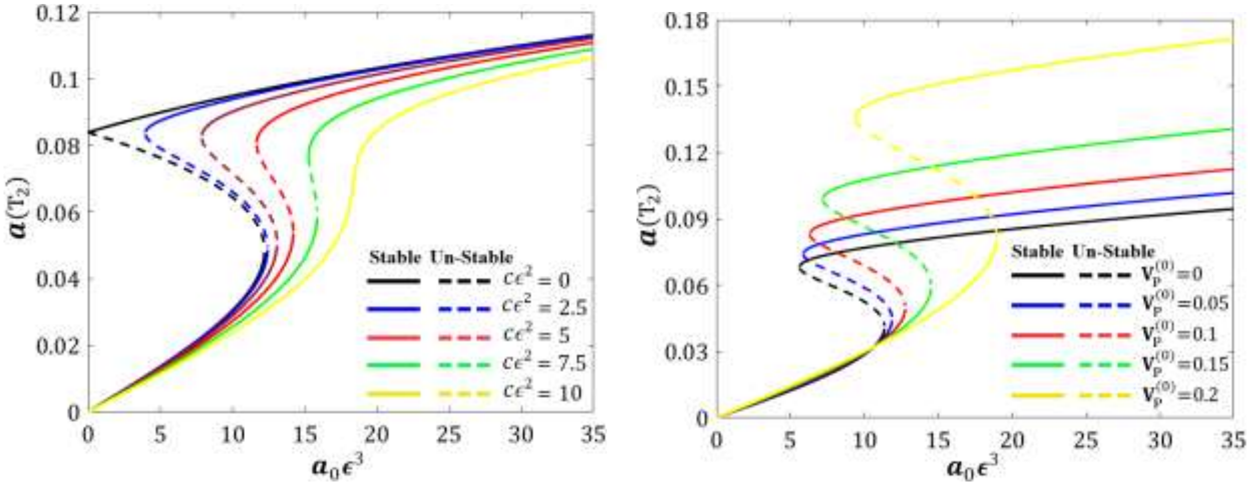

(**a**) (**b**)

Fig. **9**: acceleration response for: (**a**) six values of the perturbed damping $c\epsilon^2$,
(**b**) six values of the initial porosity volume fraction $\forall_p^{(0)}$.

To fully study the effects of initial porosity volume fraction and the dimensionless biasing voltage, ($\forall_p^{(0)}$, V), on the resonance amplitude, figure (**10-a**) has been plotted. The figure illustrates that increasing the $\forall_p^{(0)}$ and V exhibits similar characteristics, which results in an increase in both the non-trivial stable solution and the unstable solution for resonance amplitude. This means that in such a bi-stable region, the non-linear response of the system will gravitate towards one of the stable solutions based on the given initial conditions. Figure (**10-b**) shows the two-dimensional variations of resonance amplitude surfaces versus the initial porosity volume fraction and dielectric coefficient of the hydrogel layer. In region **I**, for $0 \leq \forall_p^{(0)} \leq 0.2$ and $15 \leq k_s \leq 25$, there will only one non-trivial stable solution for $\boldsymbol{a}(T_2)$, in which case the microplate will oscillate with a small amplitude. This observation can be clarified by the fact that in the approximate range $0 \leq \forall_p^{(0)} \leq 0.2$ and $25 \leq k_s \leq 30$, there are two stable and one unstable non-stationary solution for $a(T_2)$ (region **II**). Therefore, in this bi-stable region, the resonance amplitude may gravitate towards one of the non-linear responses, depending on the initial conditions.

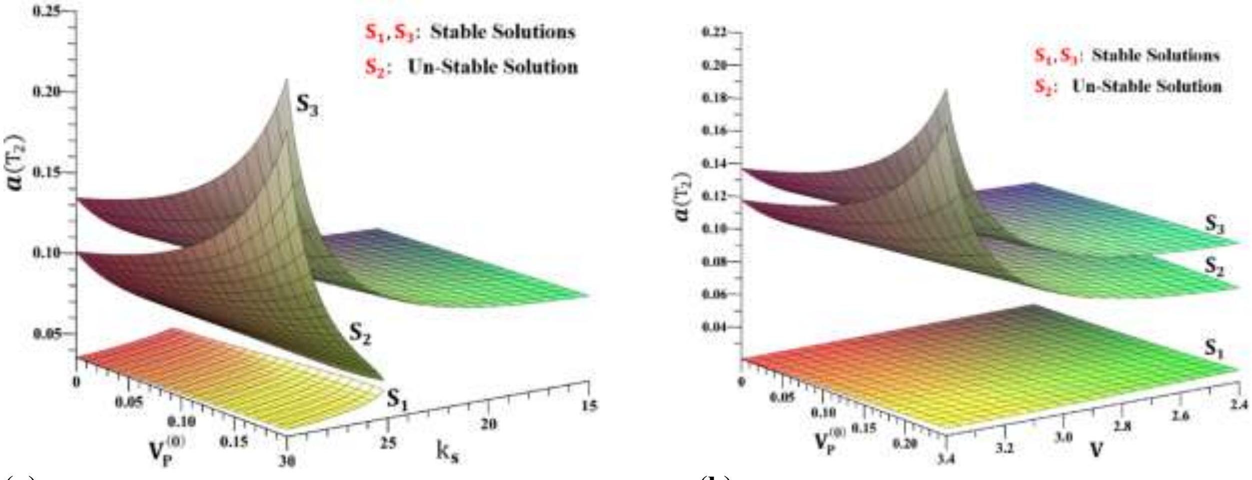

(**a**) (**b**)

Fig. **10**: (**a**). 2-Dim variation of resonance amplitude versus $\forall_p^{(0)}$ and V,

7- Conclusion

In the present work, firstly, the static pull-in behavior of an electrostatically actuated circular microplate (accelerometer sensor) resting on a porous polymeric dielectric hydrogel is investigated with respect to variations of the hydrogel layer parameters. The obtained results showed that an increase in both the dielectric coefficient, k_s, and the initial porosity volume fraction of the hydrogel layer, $\forall_p^{(0)}$, has a softening effect on the microplate and reduces the static pull-in of the microplate, whereas an increase in the initial Young's modulus of the porous hydrogel layer, $E_p^{(\mathbf{0})}$, has a hardening effect and causes the pull-in voltage to increase.

In the second stage of the present work, the non-linear lateral vibration of an accelerometer sensor subjected simultaneously to an electrostatic bias voltage and a base acceleration is studied. For this purpose, the modulation frequency and acceleration response equations are derived and solved numerically using the multiple scales method and the nonlinear trivial/nontrivial stationary solutions are obtained and their stability is analyzed in detail.

The necessary bifurcation diagrams are provided and the effects of the excitation acceleration and excitation frequency on the primary resonance of the accelerometer are studied. Also, it is showed that when the system is excited primarily and the excitation frequency lies in a specific range, the nonlinear response of the system may have dual stable non-trivial stationary coexisting solutions which will lead to the catastrophic hysteretic resonant responses. Additionally, it is showed that:

a) the resonance of the microplate is always excited, whether damping exists or not and an increase in excitation amplitude results in overall increase in the resonance amplitude.

b) Increasing the $\forall_{\boldsymbol{p}}^{(\mathbf{0})}$ not only increases the resonance amplitude, but also causes the bi-stable catastrophic hysteretic resonant region tends to increase

Author Contributions: Hamzah Kadhim Hasan was responsible for writing the original draft and generating the numerical results. Mina Ghanbari was involved in revising the manuscript and providing the numerical results. Ghader Rezazadeh supervised the project, conceptualized the methodology, and performed the modeling, review, and editing.

Data Availability Statement: The datasets generated and analyzed during the current study are available from the corresponding author upon reasonable request.

Conflicts of Interest: The authors have no conflicts of interest to declare

References

[1] Mazzei M, Lellis A.M.D. 2023. Capacitive accelerometers at low frequency for infrastructure monitoring, Procedia Structural Integrity, 44: 1212-1219

[2] Ghemari Z, Belkhiri S, Saad S. 2023. A capacitive sensor with high measurement accuracy and low electrical energy consumption, Applied Physics A, 128(362) https://doi.org/10.1007/s00339-023-06644-8

[3] Ghemari Z, Saad S. 2019. Enhancement of capacitive accelerometer operation by parameters improvement, International Journal of Numerical Modelling Electronic Networks, Devices and Fields, 32(3):e2568

[4] Ghanbari M, Rezazadeh G, Tolkani V.M, Sheikhlou M. 2023. Dynamic Analysis of a novel wide-tunable microbeam resonator with a sliding free-of-charge electrode, Nonlinear Dynamics, 111:8039-8060

[5] Shariati, A., Azaribeni, A., Hajighahramanzadeh, P., & Loghmani, Z. (2013). Liquid–liquid equilibria of systems containingsunflower oil, ethanol and water. APCBEE procedia, 5, 486-490.

[6] Ghanbari M, Rezazadeh G. 2021. Estimating the effective quality factor of a rotary comb-drive microresonator based on a neoclassical theory, Microsystem Technologies, 27(9): 3533-3543

[7] Zhao w, Alcheikh N, Ben Mbarek S, Younis M.I. 2022. Multi-functional resonant micro-sensor for simultaneous magnetic, CO2, and CH4 detection, Journal of Applied Physics, 132(14):144502

[8] Rezazadeh G, Ghanbari M, Mirzaee I. 2009. Simultaneous measurement of fluids viscosity and density using a micromeam, 5th International Conference on Perspective Technologies and Methods in MEMS Design, Lviv, Ukraine, 36-44

[9] Ghanbari M, Rezazadeh, G. 2021. A MEMS-based methodology for measurement of effective density and viscosity of nanofluids, European Journal of Mechanics B/Fluids, 86:67-77

[10] Vishnampet D.S, Yenuganti S, Paliwal S et al. 2024. Design and simulation of a resonance-based MEMS viscosity sensor, Journal of computational Electronics, 23:122-130

[11] Rao K.S, Samyuktha W, Vardhan D.V, Naidu B.G et al. 2020. Design and sensitivity analysis of a capacitive MEMS pressure sensor for blood pressure measurement, Microsystem Technologies, 26:2371-2379

[12] Kayed M. O, Balbola A.A, Lou E, Moussa W. A. Development of MEMS-based piezoresistive 3D stress/strain sensor using strain technology and smart temperature compensation, Journal of Micromechanics and Microengineering, 31:035010

[13] Ghanbari M, Rezazadeh G. 2020. A liquid-state high sensitive accelerometer based on a micro-scale liquid marble, Microsystem Technologies, 26:617-623

[14] Zhang S, Luo S, He S, Ouakad H.M. 2022. Analog circuit implementation and adaptive neural backstepping control of a network of four Duffing-type MEMS resonator with mechanical and electrostatic coupling, Chaos, Solitons & Fractals, 162: 112534

[15] Li F, Luo S, Yang G, Ouakad H.M. 2023. Dynamical analysis and accelerated adaptive bachstepping funnel control for dual-mass MEMS gyroscope under event trigger, Chaos, Solitons & Fractals,168: 113116

[16] Ramakrishnan J, Rushanth Gaurav P.T, Subash Chandar N, Sudharsan N.M. 2021. Structural design, analysis and DOE of MEMS-based capacitive accelerometer for automotive air bag application, Microsystem Technologies, 27:763-777

[17] Thu P.S, Kalugin V.V, Kochurina E.S, Ta T. 2024. Structural design and modelling of MEMS-based single axes capacitive accelerometer, Conference of Young Researchers in Electrical and Electronic Engineering (EICon), Saint Petersburg, Russian Federation,559-564

[18] Khouqeer G.A, Suganthi S, Alanazi N, Alodhayb A et al. 2023. Design of MEMS capacitive comb accelerometer with perforated proof mass for seismic applications, Journal of King Saud University-Science, 35(3):102560

[19] Ghanbari M, Rezazadeh G, Tolkani V.M. 2023. Nonlinear Dynamics of a tunable novel accelerometer, tunable with a microtriple electrode variable capacitor, Acta Mechanica, 234:3197-3218

[20] Koochaksaraie R.A, Barazande F, Barati H. 2023. A novel design of capacitive MEMS multi-range accelerometer; FEM and numerical approach, Physica Scripta, 98:115026

[21] Liu W, Zhao T, He Z, Ye J, Gong S et al. 2023. The high-efficiency design method for capacitive MEMS accelerometer, Micromachines, 14(10): 1891

[22] Guo Y, Ma Z, Zhang T, Zheng X, Jin Z. 2021. A stiffness-tunable MEMS accelerometer, Journal of Micromachines and Microengineering, 31:025005

[23] Li H, Luo R, Hu J, Yang K, Du B, Zhou S, Zhou X. 2024. Self-assembled gel-assisted preparation of high-performance hydrophobic PDMs@MWCNTS/PEDOT:PSS composite aerogels for wearable piezoresistive sensors, Journal of Materials Science and Technology, 182(20):22-32

[24] Guo Z, Zheng Y, Yin L, Xue S, Ma L et al. 2024. Flexible Au@AgNRs/MAA/PDMS-based SERS sensor coupled with intelligent algorithms for in-situ detection of thiram on apple, Sensors and Actuators B:Chemical, 404:135303

[25] Zhang H, Chen X, Liu Y, Yang C, Liu W et al. 2024. PDMS film-based flexible pressure sensor array with surface protruding structure for human motion detection and wrist posture recognition, Applied Materials @ Inerfaces, 16(2):2554-2563

[26] Fernandez F.D.M, Kim M, Yoon S, Kim J. 2024. Capacitive BaTiO3-PDMS hand-gesture sensor:Insights into sensing mechanisms and signal classification with machine learning, Composites Science and Technology, 251(26):110581

[27] Lotters J.C, Bomer J.G, Verloop A.J, Droog E.A et al. 1998. Design, fabrication and characterization of a highly symmetrical capacitive triaxial accelerometer, Sensors and Actuators A: Physical, 66(1-3):205-212

[28] Phan K.L, Mauritz A, Homburg F.G.A. 2008. A novel elastomer-based magnetoresistive accelerometer, Sensors and Actuators A: Physical, 145:109-115

[29] Huang J, Yang X, Liu J, Her S.C, Guo J et al. 2020. Vibration monitoring based on flexible multi-walled carbon nanotube/polydimethylsiloxane film sensor and the application on motion signal acquisition, Nanotechnology, 31:335504

[30] Heo Y.H, Choi D.S, Kim D.E, Kim S.Y. 2021. Flexible vibrotactile actuator based on dielectric elastomer for smart handheld devices, Applied Sciences, 11(24):12020.

[31] Nayfeh A H and Pai P F 2004 Linear and Nonlinear Structural Mechanics (New York: Wiley) pp 501, 503.

[32] Gregory W Vogl and Ali H Nayfeh, A reduced-order model for electrically actuated clamped circular plates, J. Micromech. Microeng. 15 (2005) 684–690.